

## THE ANGULAR CLUSTERING OF WISE-SELECTED AGN: DIFFERENT HALOES FOR OBSCURED AND UNOBSCURSED AGN

E. DONOSO<sup>1,2</sup>, LIN YAN<sup>3</sup>, D. STERN<sup>4</sup>, R. J. ASSEF<sup>4,5,6</sup>

<sup>1</sup>Instituto de Ciencias Astronómicas, de la Tierra, y del Espacio (ICATE), 5400, San Juan, Argentina

<sup>2</sup>Spitzer Science Center, California Institute of Technology, Pasadena, CA 91125, USA

<sup>3</sup>Infrared Processing and Analysis Center, Department of Astronomy, California Institute of Technology, Pasadena, CA 91125, USA

<sup>4</sup>Jet Propulsion Laboratory, California Institute of Technology, Pasadena, CA 91109, USA

<sup>5</sup>NASA Postdoctoral Program Fellow and

<sup>6</sup>Núcleo de Astronomía de la Facultad de Ingeniería, Universidad Diego Portales, Av. Ejército 441, Santiago, Chile

*Draft version April 17, 2014*

### ABSTRACT

We calculate the angular correlation function for a sample of  $\sim 170,000$  AGN extracted from the *Wide-field Infrared Survey Explorer* (*WISE*) catalog, selected to have red mid-IR colors ( $W1 - W2 > 0.8$ ) and  $4.6 \mu\text{m}$  flux densities brighter than  $0.14 \text{ mJy}$ . The sample is expected to be  $> 90\%$  reliable at identifying AGN, and to have a mean redshift of  $\langle z \rangle = 1.1$ . In total, the angular clustering of *WISE* AGN is roughly similar to that of optical AGN. We cross-match these objects with the photometric SDSS catalog and distinguish obscured sources with  $r - W2 > 6$  from bluer, unobscured AGN. Obscured sources present a higher clustering signal than unobscured sources. Since the host galaxy morphologies of obscured AGN are not typical red sequence elliptical galaxies and show disks in many cases, it is unlikely that the increased clustering strength of the obscured population is driven by a host galaxy segregation bias. By using relatively complete redshift distributions from the COSMOS survey, we find obscured sources at  $\langle z \rangle \sim 0.9$  have a bias of  $b = 2.9 \pm 0.6$  and are hosted in dark matter halos with a typical mass of  $\log(M/M_{\odot} h^{-1}) \sim 13.5$ . In contrast, unobscured AGN at  $\langle z \rangle \sim 1.1$  have a bias of  $b = 1.6 \pm 0.6$  and inhabit halos of  $\log(M/M_{\odot} h^{-1}) \sim 12.4$ . These findings suggest that obscured AGN inhabit denser environments than unobscured AGN, and are difficult to reconcile with the simplest AGN unification models, where obscuration is driven solely by orientation.

*Subject headings:* infrared: galaxies — galaxies: active — surveys

### 1. INTRODUCTION

In recent years, a large body of evidence suggests that the evolution and properties of active galactic nuclei (AGN) are tightly linked not only to the properties of their hosting galaxies, but also to the environment that these host galaxies inhabit. The most clear example of this perhaps comes from radio-loud AGN, which have long been known to be primarily hosted by giant, massive, elliptical galaxies, which are predominantly found in very dense environments (Matthews, Morgan & Schmidt 1964; Best et al. 2005; Donoso et al. 2010; Wylezalek et al. 2013). In general, X-ray AGN have also been found to be strongly clustered (Gilli et al. 2005; Georgakakis et al. 2007; Coil et al. 2009), though X-ray AGN out to  $z \sim 1$  with harder X-ray spectra, e.g., type-2, or obscured X-ray AGN, are preferentially found in underdense regions (Tasse, Röttgering & Best 2011).

Large redshift surveys such as the Sloan Digital Sky Survey (SDSS, York et al. 2000) and the 2dF QSO Redshift survey (Croom et al. 2004) have enabled detailed studies of optical quasars, and have shown that their clustering was larger in the past in such a way that optically selected quasars seem to be hosted by halos of roughly constant mass, a few times  $10^{12} M_{\odot}$ , out to  $z \sim 3 - 4$ .

The advent of the *Spitzer Space Telescope* opened a new, mid-infrared (mid-IR) window to AGN populations, providing samples that are relatively insensitive to the dust extinction that affects quasar surveys in the optical, ultraviolet (UV) and soft X-ray ( $< 10 \text{ keV}$ ) bands.

Stern et al. (2005) developed a simple selection technique based on IRAC colors that identifies luminous AGN essentially independent of their obscuration, and thus is particularly useful for identifying the dominant population of obscured AGN that were largely missed in previous surveys (see also Lacy et al. 2004; Donley et al. 2012). However, it is the recent launch of the *Wide-field Infrared Survey Explorer* (*WISE*; Wright et al. 2010) that has made it possible to efficiently and robustly recover AGN over the entire sky, including both unobscured and obscured sources.

The most widely accepted idea about the physical origin of obscuration is the presence of a thick dust torus that, when viewed sideways, blocks the central part of the AGN and hides many of the quasar-like features observed in unobscured AGN (Antonucci 1993; Urry & Padovani 1995). The first indirect evidence in favor of a torus was the detection of polarized broad emission lines, characteristic of unobscured AGN, in a fraction of well known obscured AGN due to the scattering toward the line of sight by free electrons just above (or below) the torus (see Heisler, Lumsden & Bailey 1997). As an alternative to orientation-driven or torus models of AGN obscuration, it is also plausible that at least part of obscuration could be caused by the interstellar medium (ISM) of the host galaxy or by larger,  $\sim \text{kpc}$ -scale clouds of cool dust (e.g., Martínez-Sansigre et al. 2009). Specifically, galaxy formation simulations by Hopkins et al. (2008) predict enhanced AGN activity after galaxy mergers, which is initially obscured by  $\text{kpc}$ -scale dust clouds but is later

laid bare as AGN feedback pushes out the obscuring material.

A basic prediction of the orientation-driven AGN unification models is that similarly selected AGN should populate similar environments. While some differences are clearly evident based on intrinsic AGN luminosity or radio-loudness (e.g., Donoso et al. 2010; Falder et al. 2010), the expectation is that obscured (or type-2) and unobscured (or type-1) AGN of similar luminosity and radio power should reside in similar environments. However, relatively little is known about the clustering of obscured AGN, particularly those identified at mid-IR wavelengths. Gilli et al. (2009) studied the spatial clustering of X-ray AGN at  $z \sim 1$ , finding no significant difference in clustering strength between obscured and unobscured X-ray selected AGN. Similarly, from a matched sample of powerful radio-loud AGN at  $1 < z < 3$ , Wylezalek et al. (2013) found that radio-loud quasars (e.g., unobscured radio-loud AGN) reside in similar environments to high-redshift radio galaxies (e.g., obscured radio-loud AGN). In contrast, Hickox et al. (2011) analyzed a sample of 806 *Spitzer* mid-IR-selected quasars at  $0.7 < z < 1.8$  in the Boötes field. They found marginal ( $< 2\sigma$ ) evidence that obscured quasars have a larger bias and populate more massive dark matter halos.

These studies, while powerful due to the availability of spectroscopic redshifts and/or a large number of photometric bands, suffer the typical limitations of deep pencil-beam surveys, providing samples of a few hundred objects at most. In this paper we adopt a complementary approach by combining the *WISE* and SDSS data sets over thousands of square degrees. We select AGN based on the *WISE* 3.4  $\mu\text{m}$  (*W1*) and 4.6  $\mu\text{m}$  (*W2*) bands using selection criteria recently developed and demonstrated by Stern et al. (2012) and Assef et al. (2013). To quantify the clustering, we undertake a correlation analysis, which is arguably the most powerful method for studying the distribution of galaxies. The angular correlation function measures the projected clustering of galaxies by comparing the distribution of galaxy pairs relative to that of a random distribution. While a less direct probe than the spatial correlation function,  $\xi(r)$ , the angular correlation function is a powerful approach as it can be applied to wide-area surveys and large samples of galaxies, overcoming the limitations of small number statistics and cosmic variance. In this work we focus on the angular correlation of AGN. Adopting a preliminary estimate of the redshift distribution of *WISE*-selected AGN, we derive the absolute bias and estimate the typical mass of the dark matter halos that host them.

This paper is organized as follows. In §2 we describe the surveys used in this work. In §3 we describe mid-IR selection of AGN using the *WISE* survey and detail the colors, morphologies, and redshift distribution of such sources. Section 4 presents the angular clustering measurements, §5 presents the results and conclusions, and §6 summarizes these results and discusses the implications of this work.

Throughout the paper we assume a flat concordance  $\Lambda\text{CDM}$  cosmology, with  $\Omega_m = 0.3$ ,  $\Omega_\Lambda = 0.7$ , and  $H_0 = 70 \text{ km s}^{-1} \text{ Mpc}^{-1}$ . Unless otherwise noted, all magnitudes in this paper refer to the Vega system.

## 2. DATA

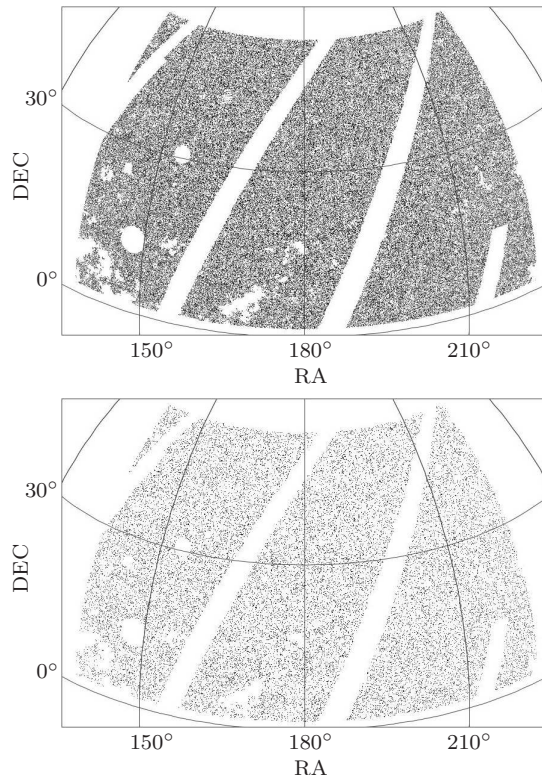


FIG. 1.— Equatorial coordinates of *WISE* AGN projected onto the celestial sphere after the masking procedure described in §4.1 to remove areas with data of compromised quality (i.e., around Moon trails, large sources, bright stars, and areas of high Galactic absorption). The top panel shows all AGN candidates with  $W1 - W2 > 0.8$  and  $W2 < 15.05$ , while the bottom panel shows *WISE* AGN lacking optical counterparts in SDSS. No obvious large-scale differences are evident, suggesting the latter are not related to Galactic sources, extinction or image artifacts.

### 2.1. Wide-field Infrared Survey Explorer

The *WISE* satellite mapped the full sky in four bands centered at 3.4, 4.6, 12 and 22  $\mu\text{m}$  (bands *W1*, *W2*, *W3* and *W4*, respectively), achieving  $5\text{-}\sigma$  point source sensitivities better than 0.08, 0.11, 1 and 6 mJy, respectively. Every part of the sky has been observed typically  $\sim 10$  times, except near the ecliptic poles where the coverage is much higher. Astrometric precision is better than  $0''.15$  for high signal-to-noise (SNR) sources (Jarrett et al. 2011) and the angular resolution is  $6''.1$ ,  $6''.4$ ,  $6''.5$  and  $12''$  for bands ranging from 3.4 to 22  $\mu\text{m}$ .

This paper is based on data from the *WISE* All-sky Release, which comprises images and four-band photometry for over 563 million sources, and has been publicly available since March 2012. An object is included in this catalog if it: (1) is detected with  $\text{SNR} > 5$  in at least one of the four bands; (2) can be measured well in at least five frames; and (3) is not flagged as a spurious artifact in at least one band. We refer the reader to the *WISE* All-sky Release Explanatory Supplement for further details<sup>1</sup> (Cutri et al. 2011).

### 2.2. Sloan Digital Sky Survey Catalog

The SDSS (York et al. 2000; Stoughton et al. 2002) is a five-band photometric (*ugriz* bands) and spectro-

<sup>1</sup> *WISE* data products and documentation are available at <http://irsa.ipac.caltech.edu/Missions/wise.html>.

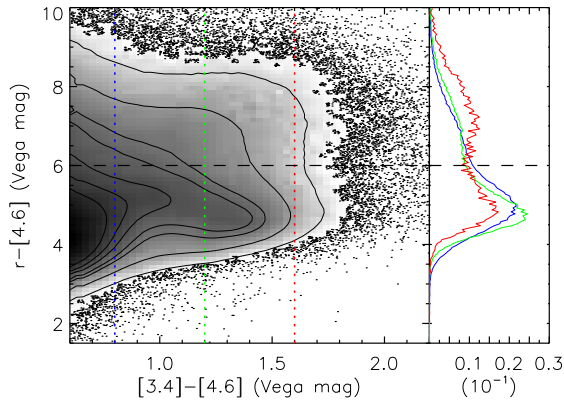


FIG. 2.— *WISE*-selected AGN split into red (e.g., obscured) sources with  $r - W2 > 6$  and unobscured AGN with  $r - W2 \leq 6$ . The grey-scale, contoured region corresponds to high-density regions, while individual points are shown in areas of low density. Histograms on the right panel illustrate the marked bi-modality of the distribution at increasingly redder colors, indicated by the vertical dotted lines in the left panel.

scopic survey that has mapped a quarter of the sky, providing photometry, spectra and redshifts for about a million galaxies and quasars, and photometry for many more. The imaging reaches 50% completeness at  $r = 22.6$  (Abazajian et al. 2009). The SDSS pipeline calculates several kinds of magnitudes. In this work we have adopted the model magnitudes (*modelMag*), which perform well for both bright and faint sources and provide unbiased galaxy colors. Magnitudes are corrected for Galactic reddening using the dust maps of Schlegel, Finkbeiner & Davis (1998). When appropriate, SDSS magnitudes (nearly in the AB system) are converted into the Vega system using  $m_{AB} = m_{Vega} + t$ , where  $t$  is estimated by projecting model stellar spectra into the SDSS  $r$ -band filter (for details, see *kcorrect*<sup>2</sup> software). In addition, SDSS asinh scale magnitudes are converted into Pogson logarithmic scale magnitudes (see SDSS website for further details).

### 3. WISE-SELECTED AGN

#### 3.1. *WISE*-selected AGN

Mid-IR selection of AGN relies on distinguishing the characteristic rising power-law AGN spectrum from the black body spectrum of stellar populations, which peak at rest-frame  $1.6 \mu\text{m}$ . This means that AGN tend to be redder than normal galaxies in the mid-IR. This was initially shown in *Spitzer* data where simple IRAC-band color cuts isolate AGN from other galaxy populations at  $z \lesssim 3$  (e.g., Lacy et al. 2004; Stern et al. 2005). More recently, the *WISE* survey has proven very efficient in detecting AGN using just the two shorter (and more sensitive) bands at  $3.4 \mu\text{m}$  and  $4.6 \mu\text{m}$  (Stern et al. 2012; Assef et al. 2013). Using empirical AGN and galaxy spectral templates, Assef et al. (2010) showed that even pure AGN present typically red  $W1 - W2$  colors out to  $z \lesssim 3.5$  for reasonable values of dilution by the host galaxy light (e.g., see Fig. 1 of Stern et al. 2012). Heavily extinguished AGN are of course even redder in  $W1 - W2$ . This contrasts with the bluer  $W1 - W2$  colors of: (1) Galactic stars, as only brown dwarfs with spectral types cooler than T5 have  $W1 - W2 > 0.8$  (Kirkpatrick et al.

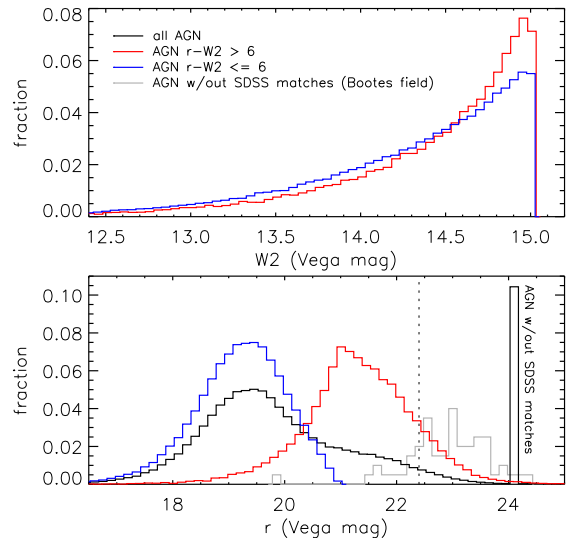


FIG. 3.— **Top:**  $W2$  magnitude distribution of *WISE* AGN candidates split into obscured ( $r - W2 > 6$ , red line) and unobscured AGN ( $r - W2 \leq 6$ , blue line). The former sources are slightly fainter on average, but both distributions are very similar. **Bottom:** Optical  $r$ -band magnitude distribution of *WISE* AGN candidates showing the effect of the  $r - W2$  color cut. For ease of plotting, the single bin at  $r = 24$  represents AGN that lack an optical match in SDSS; recall that the 50% completeness limit of SDSS is at  $r = 22.6$  (Vega, Pogson scale; vertical dashed line). We show the  $R$ -band magnitudes for 61 such AGN that are in the deeper Boötes field (grey line); most, in fact, turn out to be brighter than  $r \sim 24$ .

2011); and (2) normal galaxies out to  $z \sim 1.2$ . Thus, the primary contaminants to the red *WISE* color selections will be the coolest brown dwarfs, which are quite rare on the sky, and galaxies at  $z \gtrsim 1.2$ , which are effectively eliminated by our brightness cut,  $W2 < 15.05$ .

Using *WISE* data over the area covered by the COSMOS survey, Stern et al. (2012) demonstrated that a simple mid-IR color criterion is extremely robust at selecting AGN candidates. Selecting sources with  $W1 - W2 > 0.8$  above the  $10\text{-}\sigma$  flux limit of  $0.16 \text{ mJy}$  at  $4.6 \mu\text{m}$  ( $W2 < 15.05$ , Vega) identifies a large population of AGN that is  $\sim 95\%$  reliable and nearly  $80\%$  complete with respect to the *Spitzer* AGN selection of Stern et al. (2005). These criteria identify  $62 \text{ AGN per deg}^2$ , as compared to the  $\sim 20$  quasars per  $\text{deg}^2$  identified by the optical SDSS quasar selection algorithm, which is sensitive to AGN of similar intrinsic luminosity (Richards et al. 2002). We construct our AGN sample by applying the same selection criteria over a much larger area covered by SDSS. In our sample, we only allow sources whose  $W1$  and  $W2$  photometry is unaffected by diffraction spikes, scattered light, persistence or optical ghosts (*ccflag* = 0 in both  $W1$  and  $W2$ ). Assef et al. (2013) reports on *WISE* selection of AGN down to  $W2 < 17.1$  in the higher ecliptic latitude, and thus deeper Boötes field. We refer the reader to their work for a useful comparison of *WISE* AGN selection at various depths. We note that, ignoring  $W1 - W2$  color for the moment, typical  $L^*$  galaxies can be observed by *WISE* up to  $z \sim 1.2$  at a  $5\text{-}\sigma$  sensitivity ( $W2 = 15.85$ ; see Fig. 6 of Yan et al. 2013). With our conservative flux density cut,  $W2 = 15.05$ , only the brightest, several  $L^*$  galaxies will be detected by *WISE* at  $z \gtrsim 1$ .

Using the selection criteria of  $W1 - W2 > 0.8$  and

<sup>2</sup> Available at <http://howdy.physics.nyu.edu/index.php/Kcorrect>



$W2 < 15.05$ , we selected 176,467 *WISE* AGN candidates over an effective area of  $3363 \text{ deg}^2$  (see §4.1 for details about the angular mask). The  $W2 < 15.05$  magnitude cut guarantees that 99.7% candidates are detected with  $\text{SNR}_{W2} > 10$  and that 99.98% have  $\text{SNR}_{W2} > 9$ , while the mean  $\text{SNR}_{W2}$  of the sample is  $\sim 20$ .

The 176,467 selected AGN candidates are cross-matched with the SDSS photometric catalog. Using a matching radius of  $1''.5$ , we find 152,672 (86.5%) *WISE* AGN candidates with single optical matches, 6095 (3.5%) sources with two or more SDSS counterparts, and 17,700 (10.0%) *WISE* AGN candidates without an optical source listed in the SDSS database. The multiple optical matches are mostly due to spurious detections of large sources split into multiple components or, in a few cases, real interacting galaxy systems. These *WISE* unresolved close galaxy pairs are on scales  $\theta < 0.001 \text{ deg}$ , well below the spatial scales relevant in this work. The clustering analysis of galaxies on such small angular scales is beyond of the scope of this paper, as it would require full knowledge of the deblending performance of the SDSS and *WISE* pipelines. Therefore, we focus here on *WISE* AGN candidates with single or no optical counterparts. Note that so far we have not applied any constraints on SDSS magnitudes, so that among the 152,672 single *WISE*-SDSS matches, about 5% are fainter than the  $r = 22.6$  50%-completeness limiting magnitude of SDSS, but are nevertheless listed in the SDSS catalog. To insure that the *WISE* AGN without SDSS counterparts are all real sources and not artifacts, we have visually inspected the *WISE* and SDSS images of 1000 randomly selected objects. We did not find any artifacts from the inspection. In addition, Figure 1 shows the equatorial coordinates of all *WISE* AGN considered in this study, as well as the *WISE* AGN lacking optical counterparts in the SDSS database. In this latter case, we have closely inspected their spatial distribution projected on the sky. There are no obvious large scale patterns, suggesting that the lack of an optical identification is intrinsic to the sources, and not related to image artifacts, Galactic objects, or large-scale extinction.

Finally, to further demonstrate that the *WISE* AGN selection is robustly identifying AGN, we investigate the fraction of *WISE*-selected AGN with X-ray counterparts in the 60 ks exposures of the *XMM-Newton* wide-field ( $\sim 2 \text{ deg}^2$ ) survey of the COSMOS field (XMM-COSMOS – Hasinger et al. 2007; Brusa et al. 2010). We find that  $\sim 75\%$  of *WISE*-selected AGN are X-ray detected, with the remaining  $\sim 25\%$  expected to be fainter and/or heavily obscured AGN missed by the *XMM-Newton* observations. Indeed, deeper *Chandra* observations of the central half of the COSMOS field (Elvis et al. 2009) detect 87% of the *WISE*-selected AGN. Similar results were found previously in Stern et al. (2012), though that work imposed an  $\text{SNR}_{W2} > 10$  cut, as opposed to the flux density cut used here.

### 3.2. Red and Blue AGN in *WISE*

As mid-IR observations are relatively insensitive to obscuration by dust and optical observations are significantly affected by dust extinction, type-2, or obscured AGN, can be isolated by comparing *WISE* and SDSS fluxes (Stern et al. 2012; Yan et al. 2013). Hickox et al. (2007, 2011) applied a similar method in the Boötes field

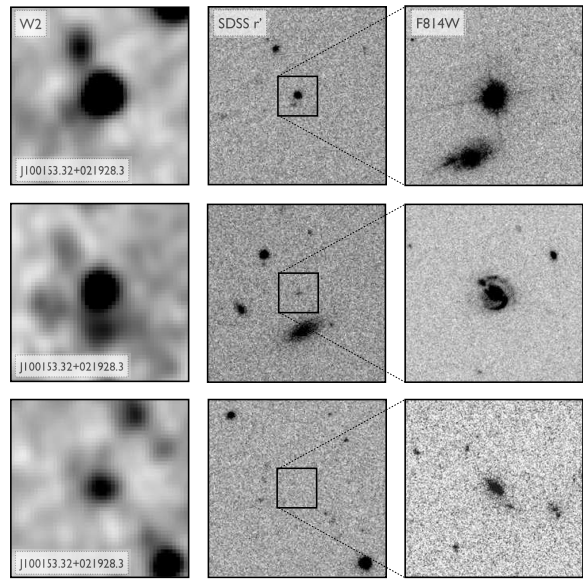


FIG. 4.— Images of three *WISE*-selected AGN in the COSMOS field, showing the range of optical morphologies. From left to right, the columns show *WISE*  $W2$  ( $\sim 1'$  on a side), SDSS  $r$  ( $\sim 1'$  on a side), and *HST*  $F814W$  ( $I_{814}$ ;  $\sim 10''$  on a side). North is up, and East is to the left. The top row shows an example of a blue, or unobscured *WISE*-selected AGN at  $z = 0.372$ . The middle row shows an example of an optically faint, red, or obscured *WISE*-selected AGN at  $z = 0.969$ ; this source is X-ray detected and classified as a type-2 AGN (Trump et al. 2007). The bottom row shows an example of the 10% of *WISE*-selected AGN that are undetected by SDSS. This source is detected by *XMM-Newton* and has a photometric redshift of  $z = 1.512$ . See text for further details on the individual sources.

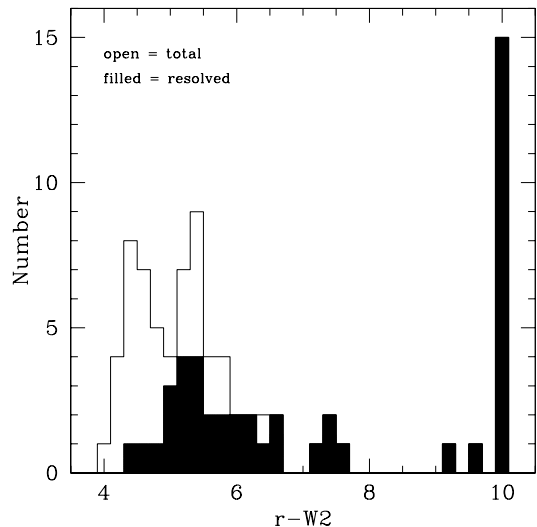


FIG. 5.— Histogram of number of *WISE*-selected AGN in the *HST*-imaged section of the COSMOS field to our  $W2 = 15.05$  depth as a function of  $r - W2$  color. The total (open + filled) histogram shows the total number of sources, while the filled histogram shows the subset that are spatially resolved by *HST*. Sources that are undetected by SDSS in the  $r$ -band are plotted at  $r - W2 = 10$ .

using IRAC  $4.5 \mu\text{m}$  and  $R$ -band photometry to differentiate obscured and unobscured AGN. For the sake of completeness, we note, however, that there is no rigorous and unique definition to differentiate obscured and unobscured AGN across all wavelengths.

In this work, we divide the *WISE* AGN sample accord-

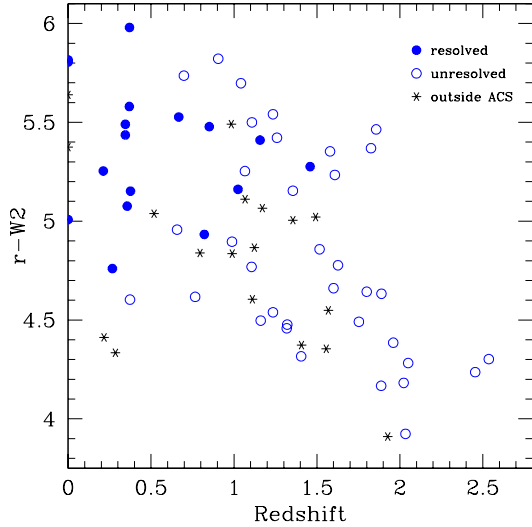


FIG. 6.—  $r - W2$  color vs. redshift for blue AGN candidates in the COSMOS field that have *HST*  $I_{814}$  morphologies available. Spatially resolved sources are indicated by filled blue symbols, while unresolved sources are marked with open symbols. A large fraction of AGN at low redshift ( $z < 0.5$ ) are clearly resolved and still meet the blue AGN selection criteria, suggesting that our low redshift, blue AGN sample is likely a mixture of obscured/unobscured AGN populations.

ing to  $r - W2$  color. Figure 2 illustrates that AGN show a bimodal color distribution that separates two populations of AGN. Those with colors redder than  $r - W2 = 6$  are, of course, optically faint (or undetected in SDSS), but nevertheless well detected at  $4.6 \mu\text{m}$ . We call these “red AGN”, in contrast with “blue AGN” that are relatively bright at both mid-IR and optical wavelengths. We fold AGN lacking optical matches into the red AGN sample. As shown in Hickox et al. (2007), the red population is more closely associated with type-2 AGN, while the blue population is associated with type-1 AGN, e.g., AGN presenting broad emission lines in optical spectroscopy. In total, about 60,000 sources are selected as red AGN candidates, implying a type-1 fraction of roughly 55%, similar to the fraction found by Assef et al. (2013) for luminous AGN with bolometric luminosities exceeding a few times  $10^{46} \text{ erg s}^{-1}$ . In §3.4 we evaluate the model selection function of red and blue AGN to test the reliability of the  $r - W2$  criteria to separate type-1 and type-2 AGN.

Figure 3 (top panel) shows the  $W2$  magnitude distribution of red and blue *WISE*-selected AGN. Although red AGN seem slightly fainter at mid-IR wavelengths in general, both subsamples have similar distributions, suggesting there is no strong bias due to the  $r - W2$  color cut. The bottom panel shows the distribution of SDSS  $r$ -band magnitudes (corrected for Galactic reddening, converted to Vega and in the Pogson scale). Blue AGN are considerably brighter, peaking at  $r \sim 19.3$  and falling steeply at  $r \gtrsim 19.5$ . Most red AGN are fainter, peaking around  $r \sim 21.2$  and extending to fainter magnitudes, beyond the nominal SDSS completeness limit. A considerable fraction (10%) of *WISE* AGN candidates are simply undetected by SDSS; we indicate such sources with a single bin at  $r = 24$ . The Boötes field has considerably deeper  $R$ -band photometry available, reaching  $R \sim 26$  ( $5\text{-}\sigma$ , point source; Jannuzi et al. 2010). There are 61

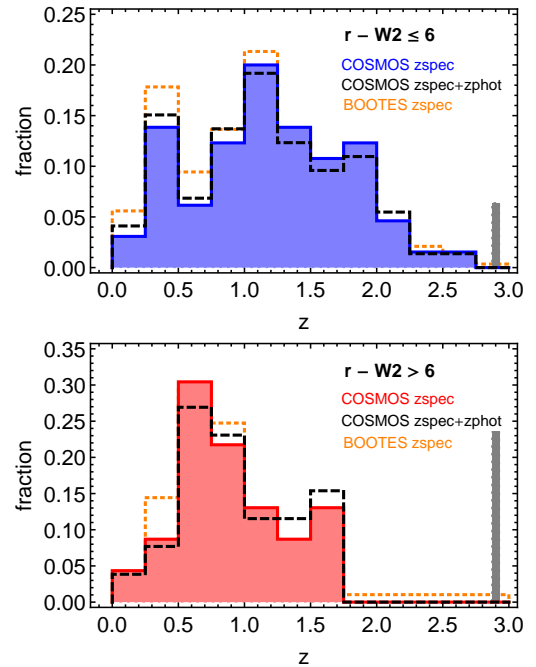


FIG. 7.— Redshift distribution of *WISE*-selected AGN in COSMOS. The top panel highlights the blue AGN ( $r - W2 \leq 6$ ), with the solid histogram showing sources with spectroscopic redshifts and the dashed histogram including five additional photometric redshifts. The five sources lacking both spectroscopic and photometric redshifts are plotted at  $z = 2.9$  (gray bar). The bottom panel highlights the red AGN, again distinguishing spectroscopic redshifts (solid histogram) and photometric redshifts (dashed). The eight sources lacking both spectroscopic and photometric redshifts are plotted at  $z = 2.9$  (gray bar). For reference, we also show in both panels the corresponding redshift distributions in Boötes (dotted orange).

SDSS-undetected, *WISE*-selected AGN in Boötes. Their  $R$ -band magnitude distribution peaks at  $R \sim 23$  (gray line) with all sources having optical counterparts. This again illustrates the optical faintness, but detectability of essentially all *WISE*-selected AGN. Finally, we note that the fraction of *WISE*-selected AGN with X-ray counterparts in the *XMM-Newton* wide-field at the 0.5–10 keV band is  $\sim 83\%$  for blue AGN ( $r - W2 \leq 6$ ), dropping to  $\sim 68\%$  for red AGN ( $r - W2 > 6$ ). These high detection rates further demonstrate the reliability of our sample.

### 3.3. Morphologies

Figure 4 shows the range of optical morphologies of *WISE*-selected AGN. For three candidates in the COSMOS field, we display  $\sim 1'$  on a side images in *WISE*  $W2$  and SDSS  $r$ -band, and  $\sim 10''$  on a side *Hubble Space Telescope* (*HST*) images in the  $F814W$  filter. The top row shows an example of a blue, or unobscured *WISE*-selected AGN: WISE J100025.25+015852.1 is an optically bright, optically unresolved SDSS quasar ( $r - W2 = 4.6$ ) at redshift  $z = 0.372$ . The middle row shows an example of an optically faint, or red, obscured *WISE*-selected AGN: WISE J100005.98+015453.1 is an optically faint source detected by SDSS ( $r - W2 = 6.7$ ). Trump et al. (2007) report a redshift of  $z = 0.969$  for this X-ray detected, optically resolved source and classify it as type-2 AGN based on its spectrum. The bottom row shows an example of the 10% of *WISE*-selected AGN which are undetected by SDSS: WISE J100153.32+021928.3 is undetected by SDSS ( $r - W2 \geq$

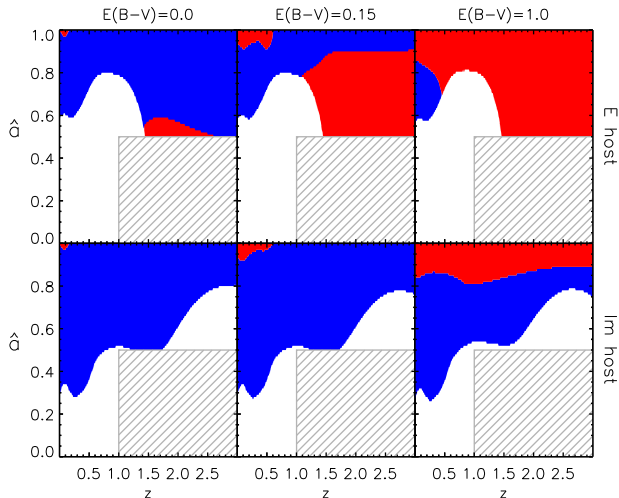


FIG. 8.— Model selection function of blue and red AGN constructed using mock objects that adopt the AGN and galaxy SED templates of Assef et al. (2010). The parameter  $\hat{a}$  is the fraction of the bolometric luminosity coming from the AGN component (see text for details). Each panel shows for a given host galaxy type (E or Im) and reddening value, whether an object would be targeted as a blue AGN (blue region), red AGN (red region), or an inactive galaxy (white region). The gray hatched area marks the region where *WISE* is not sensitive due to its shallowness given our  $W2 < 15.05$  brightness cut, namely  $z > 1$  host-galaxy dominated objects. While essentially all of the unobscured AGN (left panels) are correctly identified as blue AGN, some fraction of obscured AGN (right panels) will have blue AGN colors. Phrased differently, we expect the red AGN sample to be a relatively pure sample of obscured AGN, while the blue AGN sample will primarily be unobscured AGN, but will have some contamination from obscured sources.

7.5), but is detected by both *HST* and *XMM-Newton*. The source has a photometric redshift of  $z = 1.512$ .

Optical morphologies offer an additional observable with which to investigate the *WISE* AGN selection. Luminous, unobscured, or type-1 AGN are typically unresolved at optical wavelengths, which was one of their foundational attributes that led to the name “quasar”, or quasi-stellar radio source. We have known for several decades now that only  $\sim 15\%$  of quasars are radio-loud, with little variation in this fraction with either redshift or optical luminosity, at least at the high luminosity end (e.g., Stern et al. 2000). Similarly, mid-IR selection is showing that unresolved, unobscured quasars represent a minority population of luminous AGN. Indeed, using the SDSS type flag to discriminate morphologies, we find only  $\sim 55\%$  of the *WISE*-selected AGN considered in this paper are classified as unresolved point sources.

We use the COSMOS field to characterize how morphology depends on optical-to-mid-IR color for *WISE*-selected AGN. Figure 5 shows a histogram of the optical-to-mid-IR colors of the 82 *WISE*-selected AGN with *HST* ACS (F814W) imaging in COSMOS to our  $W2 = 15.05$  depth, coded by optical morphology. Fifteen of the sources are undetected by SDSS in the *r*-band, and are simply plotted at  $r - W2 = 10$ ; all 15 of these sources are detected in the deeper *HST* F814W imaging and are spatially resolved. Indeed, of the 28 red AGN candidates with  $r - W2 > 6$ , only 1 (4%) is unresolved. This supports our expectation that red optical-to-mid-IR colors select a clean sample of obscured AGN with little contamination from unobscured AGN.

Of the 54 blue AGN candidates, 35 (65%) are unre-

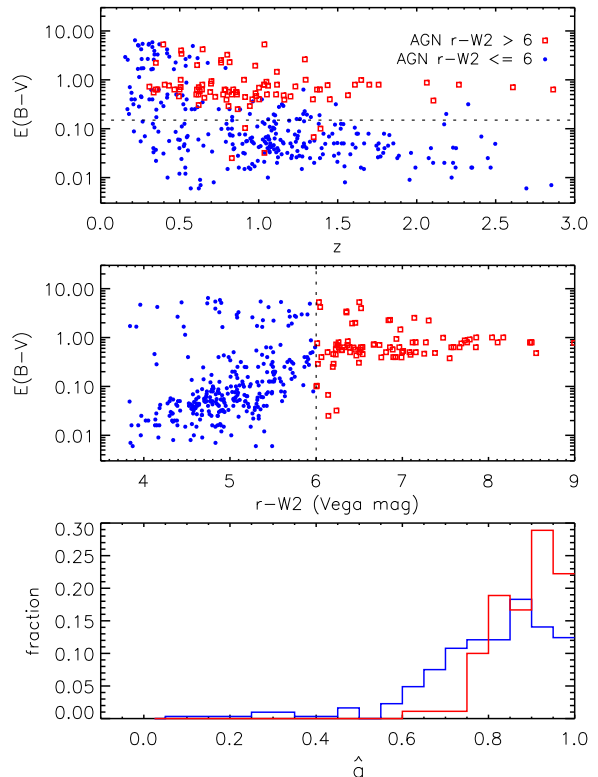


FIG. 9.— Dependence of the reddening parameter,  $E(B-V)$ , with redshift (top panel) and  $r - W2$  color (middle panel) for blue (filled symbols) and red (open squares) *WISE*-selected AGN candidates in the Boötēs field.  $E(B-V)$  is derived by fitting the AGN and galaxy SED templates of Assef et al. (2010). In general, red AGN tend to have considerable reddening at all redshifts while blue AGN are mostly unreddened at  $z > 0.5$ , but can have large reddening values at lower redshift. The fiducial type-1/type-2 separation is around  $E(B-V) = 0.15$ . The bottom panel shows the distribution of the  $\hat{a}$  parameter (see §3.4 for definition) for red and blue AGN.

solved. Figure 6 shows the  $r - W2$  color vs. redshift for these blue AGN candidates, with symbols indicating their *HST* morphologies. As we will show in the next section, most of the resolved AGN – e.g., likely obscured AGN contaminating our blue AGN selection – are at lower redshift ( $z < 0.5$ ) and, in fact, reside in the redder end of our blue AGN selection. However, Figure 5 also clearly shows that it is not feasible to simply make a bluer  $r - W2$  cut to separate obscured (e.g., resolved) and unobscured (e.g., unresolved) AGN.

To characterize the host galaxies of *WISE*-selected candidates we performed more detailed visual classifications on the *HST* ACS image cutouts (independently by three of the four authors; as we agreed for the majority of objects, we report the average here). For red AGN, we find that 54% (15) are disk galaxies or interacting systems, 32% (9) are elliptical or point sources, and the remaining 14% (4) have uncertain morphology. This contrasts with blue AGN, where we find that 20% (11) are disk galaxies and 80% (43) are either point sources (most) or ellipticals. These results are consistent with the work of Griffith & Stern (2010), who studied the morphology of AGN in COSMOS selected at radio, X-ray and mid-IR wavelengths. That work found that the red mid-IR-selected AGN consist of 63% disk galaxies, 22% point sources/ellipticals, and 15% other morphology, while the blue AGN consist of 15% disk galaxies



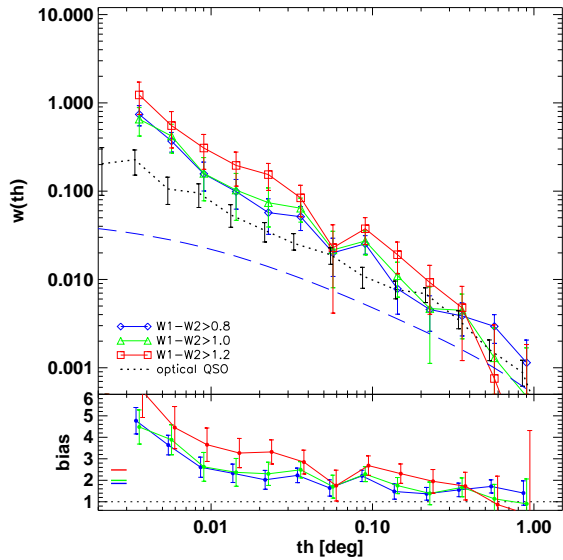


FIG. 10.— Angular correlation function  $w(\theta)$  of *WISE*-selected AGN with increasingly red  $W1 - W2$  color cuts. For reference, we also show data for optical quasars at  $z_{\text{phot}} < 2.3$  from Myers et al. (2007, dotted line). Model predictions for the dark matter angular correlation function,  $w_{\text{dm}}(\theta)$  (dashed line) are computed using the Peacock & Dodds (1996) fitting function and the same AGN redshift distribution as the  $W1 - W2 > 0.8$  sample. The bottom panel shows the absolute bias  $b = \sqrt{w/w_{\text{dm}}}$ . Markers on the left indicate the mean bias value over the range 0.02-0.4 deg.

and 85% point sources/ellipticals. The main conclusion we wish to draw here is that given its high fraction of disk galaxies, the red AGN sample is not dominated by typical red sequence galaxies. In fact, the red AGN have a higher fraction of disk galaxies than the blue AGN. As further discussed in §5.3, this suggests it is unlikely that a bias in host galaxy type (favoring red AGN in early-type hosts and blue AGN in late-type hosts) could have a large impact in the interpretation of the clustering results presented in §5.

#### 3.4. Redshift Distribution and Selection Function

Given the difference in optical flux introduced by the  $r - W2$  cut, it is not unreasonable to expect differences in the redshift distribution of blue and red AGN. In order to understand the redshift distribution and properties of *WISE* AGN candidates, we have matched our list to publicly available spectroscopy in the COSMOS field as well as recent spectroscopic observations (see Stern et al. 2012 for details about the compiled list of spectroscopic and photometric redshifts).

Figure 7 shows the redshift distribution of the 112 *WISE*-selected AGN available in COSMOS, of which 88 have spectroscopic redshifts and 11 have photometric redshifts (plus 13 objects with no redshift information available). The top panel highlights the blue AGN ( $r - W2 \leq 6$ ), including five sources, plotted at  $z = 2.9$ , that lack both spectroscopic and photometric redshifts. The distribution peaks around  $z \sim 1.1$  and extends up to  $z \sim 2.5$ , with most of the sources at  $0.8 < z < 2$ . There is an indication of a second smaller peak at  $z \sim 0.5$ , most probably (as we will see later) due to type-2 AGN that enter into the redder part of our blue sample selection at low redshift. For reference, we also show the spectroscopic redshifts of 536 *WISE* AGN candidates within the Boötes field (dashed histogram), obtained from the AGN

and Galaxy Evolution Survey (AGES; Kochanek et al. 2012). This survey has different completeness levels for different galaxy samples ( $I < 20$  for galaxies,  $I < 22.5$  for AGN, but with varying priority levels based on their brightness at mid-IR,  $24\mu\text{m}$ , radio, and X-ray energies) and therefore a complicated redshift selection function. However, considering the differences in target selection as compared to COSMOS (which essentially targeted every source to  $R \sim 25$ ), the two distributions agree remarkably well. This suggests that both are not far from the true redshift distribution of *WISE*-selected AGN with blue  $r - W2$  colors. The bottom panel in Figure 7 shows the corresponding distributions for *WISE*-selected AGN with red  $r - W2$  colors, including eight sources lacking both spectroscopic and photometric redshifts plotted at  $z = 2.9$ . Red AGN candidates peak at lower redshift, around  $z \sim 0.8$ , and extend up to  $z \sim 1.8$ . Again, the agreement with AGES redshifts in the Boötes field is notable.

To further understand the nature of the differences in redshift among the red and blue AGN samples, we model their selection function by constructing mock objects using the AGN and galaxy spectral energy distribution (SED) templates from Assef et al. (2010). The parameter  $\hat{a} \equiv L_{\text{AGN}}/(L_{\text{host}} + L_{\text{AGN}})$  quantifies the fraction of the bolometric luminosity coming from the AGN component (see Assef et al. 2010, 2013 for details). Figure 8 shows whether an object with a given host galaxy type (E or Im),  $\hat{a}$  value, and reddening towards the accretion disk, parametrized by  $E(B - V)$ , would be targeted as a blue AGN ( $r - W2 \leq 6$ , blue region), as a red AGN ( $r - W2 > 6$ , red region), or as an inactive galaxy ( $W1 - W2 < 0.8$ , white region). As expected, at low  $\hat{a}$ , most systems are characterized as normal galaxies. The panels at  $E(B - V) = 0.0$  and  $E(B - V) = 1.0$  highlight the extreme cases of a zero reddening or a heavily extinguished AGN; the typical boundary between type-1 and type-2 AGN corresponds to a reddening of  $E(B - V) = 0.15$  (see Assef et al. 2013 for details). The gray hatched area marks the region where *WISE* is not sensitive due to the shallowness imposed by our  $W2 < 15.05$  flux density requirement, namely  $z \gtrsim 1$  host-galaxy dominated objects. This figure shows that while it is very unlikely to misclassify a blue AGN as a red one, the opposite happens for a significant fraction of parameter space, suggesting that our red AGN selection constitutes a reliable yet incomplete type-2 AGN sample, while our blue sample consists of a mixture of type-1 and type-2 AGN.

We also used the deep, multi-wavelength data available in the Boötes field to do detailed SED modeling of *WISE*-selected AGN and explore how reddening relates to  $r - W2$  color for blue and red AGN candidates as a function of redshift. This is shown in Figure 9. The reddening parameter  $E(B - V)$  is derived by fitting the AGN and galaxy SED templates of Assef et al. (2010). As expected, red AGN tend to show considerable reddening at all redshifts, with  $E(B - V) \gtrsim 0.7$ , while blue AGN are mostly unreddened above  $z \sim 0.5$ . However, below this redshift, blue AGN can sometimes show large reddening values, consistent with the idea that some of these objects might well be type-2 AGN interlopers in the blue sample. As shown in the bottom panel of Figure 9, the distributions of  $\hat{a}$  are strongly peaked toward high values,

with most red AGN above  $\hat{a} \sim 0.8$ , and a minor fraction of blue AGN with  $0.6 < \hat{a} < 0.8$ . This means that while the blue area in the bottom right panel of Figure 8 is large, only a minority of sources could be potentially biased due to the galaxy host type (i.e. selected as blue AGN due to the presence of Im galaxy host).

#### 4. ANGULAR CORRELATION ANALYSIS

##### 4.1. The Angular Correlation Function

A standard tool to measure galaxy clustering is the two-point angular correlation function,  $w(\theta)$ . It is defined as the probability that a given pair of galaxies separated by an angle  $\theta$  on the sky are contained within a solid angle  $d\omega$

$$dP = n(1 + w(\theta))d\omega, \quad (1)$$

where  $n$  is the mean number density of galaxies. In practice,  $w(\theta)$  is calculated by counting pairs of galaxies in annuli of different radii and comparing with the corresponding counts in a random sample of galaxies. To estimate  $w(\theta)$  we use the Landy & Szalay (1993) estimator, given by

$$w(\theta) = \frac{DD - 2DR + RR}{RR}, \quad (2)$$

where  $DD$ ,  $DR$  and  $RR$  are the normalized data-data, data-random and random-random pair counts, respectively. It is very important that the random sample has the same angular selection as the data pairs. For this purpose we constructed an angular mask using the software `mangle`<sup>3</sup> that describes the survey geometry in terms of disjoint spherical polygons. This mask accounts for the holes caused by bad quality fields in the SDSS survey, as well as the areas around bright stars selected from the Tycho 2 catalog ( $BTMAG < 11.5$ ). In addition, we also remove the areas around large ( $> 2''$ ) sources from the 2MASS Extended Source Catalog that in some cases appear decomposed into multiple sources in *WISE*. Galactic absorption can have an impact in faint galaxy counts (Myers et al. 2006), so we mask out areas with  $A_g > 0.18$ . Finally, we avoid regions contaminated by the Moon and limit the sample to the rectangular area bounded by  $135^\circ < \text{R.A.} < 226^\circ$  and  $1^\circ < \text{Dec.} < 54^\circ$  (J2000). These rather conservative limits avoid both the Galactic plane, where contamination by stars could present an issue, and the ecliptic pole, where the sensitivity of *WISE* improves substantially due to denser coverage and lower zodiacal background. Our selected area has a typical *WISE* coverage of  $\sim 13$  frames per bandpass.

##### 4.2. Absolute Bias and Halo Masses of *WISE* AGN

At small scales, the clustering of an extragalactic source population is difficult to predict due to processes such as merging and interactions. However, at larger scales (e.g.,  $> 1-2 h^{-1}$  Mpc), galaxy interactions have little impact and the galaxy correlation function follows that of the dark matter halos. At any redshift, massive halos cluster more strongly than less massive halos. Given an average redshift, this, in turn, allows one to estimate the typical mass of dark matter halos in which

<sup>3</sup> Available at <http://space.mit.edu/~molly/mangle/>.

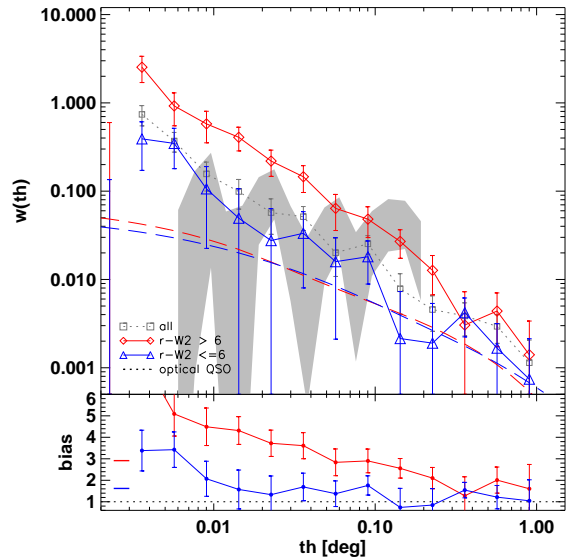


Fig. 11.— Angular correlation function  $w(\theta)$  of *WISE*-selected AGN split into obscured sources with  $r - W2 > 6$  and unobscured AGN with  $r - W2 \leq 6$ . The bottom panel shows the absolute bias with respect to the dark matter angular correlation (dashed line). Markers on the left indicate the mean bias value. The grey shaded region shows the angular autocorrelation of type-1 quasars from Hickox et al. (2011) (inferred from the quasar-galaxy and galaxy-galaxy correlation function), which is in broad agreement with our estimation for the blue AGN sample.

objects reside by estimating their absolute bias, i.e., their observed clustering level with respect to that of the underlying dark matter.

We compare our  $w(\theta)$  measurements to the predictions of the standard cold dark matter (CDM) model in the linear perturbation theory of structure growth along with the non-linear correction. To compute the dark matter angular two-point correlation function,  $w_{\text{dm}}(\theta)$ , we use the non-linear fitting function of Peacock & Dodds (1996) for the CDM power spectrum projected onto the same AGN redshift distribution. The bias factor is simply defined as  $b \equiv (w(\theta)/w_{\text{dm}}(\theta))^{1/2}$ . In general, the bias is a function of scale, but under the assumption that galaxies cluster in a similar manner as dark matter, the bias factor is nearly scale-independent. This is particularly valid in the linear regime (i.e., large scales; see Verde et al. 2002). We limit the bias and the corresponding fits from  $\theta = 0.04^\circ$  to  $\theta = 0.4^\circ$ , which corresponds to scales of roughly  $\sim 800 h^{-1}$  kpc to  $\sim 8 h^{-1}$  Mpc at  $z \sim 1.2$ .

Using an ellipsoidal collapse model, Sheth, Mo & Tormen (2001) related the halo bias factor to its mass and calibrated a fitting relation for a large library of cosmological  $N$ -body simulations:

$$b(M_{\text{halo}}, z) = 1 + \frac{1}{\sqrt{a}\delta_c(z)} [\sqrt{a}(av^2) + \sqrt{ab}(av^2)^{1-c} - \frac{(av^2)^c}{(av^2)^c + b(1-c)(1-c/2)}] \quad (3)$$

where  $a = 0.707$ ,  $b = 0.5$ ,  $c = 0.6$  and  $\delta_c(z)$  is the critical density ratio for collapse given by Navarro, Frenk & White (1997) as  $\delta_c(z) = 0.15(12\pi)^{2/3}\Omega_{mz}$ , and  $\Omega_{mz} \equiv (H_0/H(z))^2\Omega_m(1+z)^3$ .



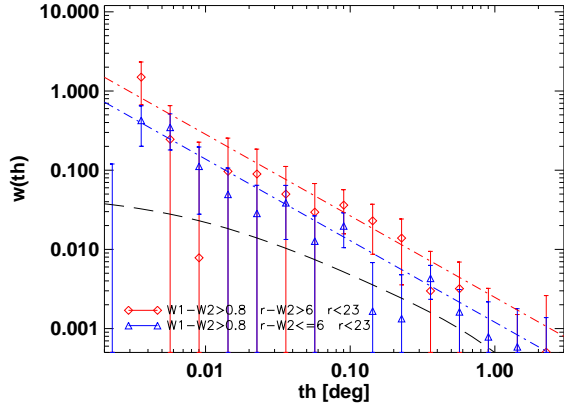


FIG. 12.— Angular correlation function  $w(\theta)$  of *WISE*-selected AGN as in Figure 11, but limited to sources with  $r$ -band counterparts brighter than  $r = 23$  in the SDSS survey. Simple power-law fits of the form  $A\theta^{-\gamma}$  (dot-dashed lines) have a correlation amplitude a factor of  $\sim 2$  larger for the obscured population compared to the unobscured sources.

$H(z)$  depends on the cosmology as  $H^2(z) = H_0^2(\Omega_m(1+z)^3 + \Omega_\Lambda)$ , and  $\nu$  is defined as  $\nu \equiv \delta_c z / \sigma(M)D(z)$ , where  $D(z)$  is the linear growth factor, here approximated analytically using the formulae by Carroll, Press & Turner (1992). The rms fluctuation of the density field is given by

$$\sigma^2(M_h) = \frac{1}{2\pi^2} \int_0^\infty k^2 P(k) \left[ \frac{3(\sin(kr) - (kr)\cos(kr))}{(kr)^3} \right] dk, \quad (4)$$

where the term in brackets represents the spherical top-hat window function (Peebles 1980) and the radius  $r$  is related to the enclosed halo mass  $M_h$  as

$$r = \sqrt[3]{\frac{3M_h}{4\pi\rho_0}}, \quad (5)$$

where  $\rho_0$  is the present mean density of the Universe, given by  $2.78 \times 10^{11} \Omega_m h^2 M_\odot \text{Mpc}^{-3}$ . The linear power spectrum of density fluctuations,  $P(k) \propto T^2(q) k^n$  with  $n=1$  (the Harrison-Zel'dovich case), is constructed using the fitting formula of Eisenstein & Hu (2001) for the transfer function  $T(k)$  and normalized with the adopted value of  $\sigma_8 = 0.84$  for  $r = 8 h^{-1} \text{Mpc}$ .

## 5. RESULTS

### 5.1. Comparison to Optically Selected Quasars

We begin our analysis by exploring the angular clustering for the full sample of AGN selected by *WISE*. Figure 10 shows that AGN with  $W1 - W2 > 0.8$  present an angular correlation similar to that of optical quasars selected from SDSS by Myers et al. (2007) using a photometric kernel density estimation (KDE) technique (Richards et al. 2004). A power-law fit of the form  $w(\theta) = A\theta^{-\gamma}$  gives a value of  $\gamma = 1.03 \pm 0.11$  within the range  $\theta = [0.02^\circ - 0.5^\circ]$  ( $\sim 0.4 - 10 h^{-1} \text{Mpc}$  at  $z = 1.1$ ). Myers et al. (2006) find  $\gamma = 0.98 \pm 0.15$  for optically selected quasars at  $z = 1.4$ , while Croom et al. (2005) find a slightly shallower value for 2QZ quasars,  $\gamma = 0.86 \pm 0.06$  when averaged over scales of  $1-100 h^{-1} \text{Mpc}$  and after correcting for redshift distortions. These slight differences are not entirely surprising considering the very different AGN selection criteria and the fact that the

*WISE* AGN sample includes both obscured and unobscured AGN, while the optical quasar samples are entirely comprised of broad-lined, type-1 AGN. Furthermore, the clustering of quasars might not be properly represented by a single power law.

At scales below  $\theta \sim 0.1^\circ$ , we find that redder AGN have slightly higher angular clustering. This is interesting considering that this scale ( $\sim 2 h^{-1} \text{Mpc}$ ) marks the transition between the 1-halo and 2-halo terms, which, in the framework of halo clustering models, arises from galaxy pairs located in either the same or in two different halos, respectively. As shown at the bottom panel of Figure 10, the absolute bias for *WISE*-selected AGN with  $W1 - W2 > 0.8$  with respect to the underlying dark matter distribution is  $b = 1.9 \pm 0.4$ , as compared to  $b = 2.5 \pm 0.6$  for *WISE*-selected AGN with redder mid-IR colors,  $W1 - W2 > 1.2$ . Taking into account the caveat that different redshift and luminosity distributions can possibly bias the results, the simplest interpretation is that redder AGN are hosted by slightly more massive dark matter halos. For type-1 AGN at  $z \lesssim 2.5$  previous work has shown that the clustering depends only weakly on redshift, luminosity or color (Shen et al. 2009; Ross et al. 2009). However, for type-2 AGN this is mostly unknown and our  $W1 - W2 > 0.8$  sample is expected to be a mixture of both type-1 and type-2 AGN. Finally, we note that our results compare well to the bias estimates obtained by Myers et al. (2007) for optical quasars over a similarly broad redshift range centered at  $\langle z \rangle = 1.4$ .

### 5.2. Clustering of Red and Blue AGN

We explore now the angular clustering of *WISE*-selected red and blue AGN. The corresponding correlation functions, shown in Figure 11, display very different amplitudes. For a fixed slope  $\gamma = 1.03$  (that of the entire AGN sample), blue, or unobscured AGN (e.g.,  $r - W2 \leq 6$ ) have  $A = 0.0010 \pm 0.0002$ , while red, or obscured AGN (e.g.,  $r - W2 > 6$ ) have  $A = 0.0039 \pm 0.0004$ , i.e., a factor of  $\sim 4$  larger. The bottom panel shows that the mean bias of obscured sources relative to the dark matter is  $b = 2.9 \pm 0.6$ , as compared to  $b = 1.6 \pm 0.6$  for unobscured AGN. For reference, we also show in Figure 11 the angular clustering of type-1 quasars (grey shaded area) from Hickox et al. (2011), which is in broad agreement with our estimation for the blue AGN sample.

Part of the difference in clustering strength could, in principle, be due to the obscured sources having a different selection, that is, since obscured sources are required to be optically faint (or undetected), they could reside at slightly higher redshifts than their unobscured cousins. On the contrary, spectroscopy from both COSMOS and Boötes demonstrates that red AGN tend to be at slightly lower redshift (Figure 7). The caveat is that there is a  $\sim 20\%$  incompleteness in the two spectroscopic samples and the sample sizes are not extremely large. While directly comparing the full and complete redshift distributions for blue and red *WISE*-selected AGN would be ideal to check whether their different clustering strengths are related to different redshift distributions, we can nevertheless minimize it by selecting AGN limited only to those with  $r < 23$  counterparts in SDSS. The amplitudes of the best-fit power-law become  $A = 0.0024 \pm 0.0006$  for obscured AGN, compared to  $A = 0.0012 \pm 0.0002$  for

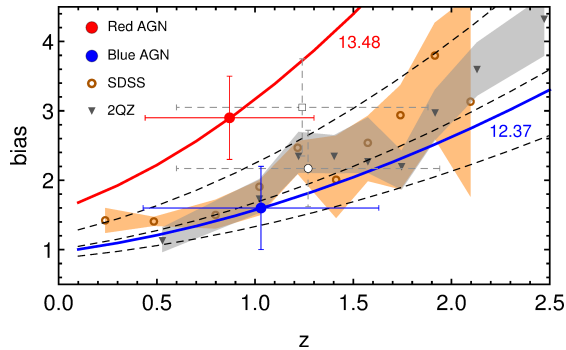


FIG. 13.— Bias as a function of redshift for *WISE* blue and red AGN, shown at the mean redshift of their corresponding best-fit distributions. For reference, we also overlay data derived from optical SDSS quasars (orange, Ross et al. 2009) and 2QZ quasars (gray, Croom et al. 2005), as well as previous results from Hickox et al. (2011) for obscured (hollow square) and unobscured AGN (hollow circle). Dashed lines are models of constant halo mass of  $\log(M/M_{\odot} h^{-1}) = 13, 12.5, 12$  (from top to bottom), while the best-fit cases for *WISE* AGN are indicated by solid, thick lines.

unobscured AGN, for a fixed slope  $\gamma = 1.03$ . Figure 12 shows the corresponding angular auto-correlations, illustrating once again that, while noisier, obscured AGN have a correlation amplitude a factor of  $\sim 2$  larger than the unobscured sources.

Given the difference in amplitude between the correlation functions of red and blue AGN, we investigate how this reflects into the masses of dark matter halos that host them. Using the prescriptions described in §4.2, we estimate that blue AGN at  $z \sim 1$  are hosted in halos of characteristic mass  $\log(M/M_{\odot} h^{-1}) = 12.37^{+0.57}_{-1.00}$ . This is in excellent agreement with the halo mass of  $\log(M/M_{\odot} h^{-1}) \sim 12.3$  reported by Ross et al. (2009) for SDSS optical quasars at  $z < 2.2$ . Croom et al. (2005) finds a similar value of  $\log(M/M_{\odot} h^{-1}) \sim 12.5^{+0.2}_{-0.3}$  for 2QZ quasars hosts. In Figure 13 we show the bias as function of redshift for the best-fit model (thick blue line), along with models of constant halo mass (dashed black lines) for reference. We find that the halos of our red AGN have a much larger characteristic mass of  $\log(M/M_{\odot} h^{-1}) = 13.48^{+0.54}_{-0.31}$ , i.e. over a factor of 10 larger than for blue AGN. We discuss the physical implications of this result in the following section. We also note that Hickox et al. (2011) reports a very similar mass of  $\log(M/M_{\odot} h^{-1}) = 13.3^{+0.3}_{-0.4}$  for their obscured quasar sample, though their value of  $\log(M/M_{\odot} h^{-1}) = 12.7^{+0.4}_{-0.6}$  for unobscured quasars is slightly larger than both our value and literature results for optically selected unobscured quasars.

### 5.3. The Host Galaxies of *WISE* AGN

To understand the clustering result of our red and blue samples, we study the host galaxies of *WISE*-selected AGN using SED fitting and the morphology classifications discussed in §3.3. This is important because the observed difference in clustering might, in principle, be attributed to a selection effect that biases our red AGN sample to being hosted by early-type galaxies and our blue AGN to being hosted by late-type galaxies. Such a difference might either be the result of an intrinsic difference between the populations or due to a selection function bias. In particular, Figure 8 suggests that our red AGN sample could be biased against type-2 quasars

in starburst galaxies if mid-IR selected AGN had a large spread over  $\hat{\alpha}$  values.

First, we use the SED fitting of *WISE*-selected AGN candidates in the Boötes field with the templates of Assef et al. (2010) to analyze the distribution of host light coming from each of the three galaxy templates (E, Sbc and Im). From Figure 9, the blue AGN sample contains some sources with considerable dust obscuration (i.e., well above the  $E(B-V) = 0.15$  boundary line). For these misclassified type-2 AGN, we find that 38%, 36% and 26% of their host galaxy emission is dominated by the E, Sbc and Im templates, respectively, where we define an object to be dominated when  $>50\%$  of the host luminosity is coming from a given template. These similar proportions suggest that this selection bias, if present, is not preferentially missing Im galaxies, and therefore it is unlikely to be significantly affecting our results. For completeness, we note that it is difficult to determine the dominant host for the majority of blue candidates which have  $E(B-V) < 0.15$  and thus AGN emission dominates the optical SED, making host SED fitting challenging.

The same analysis for red AGN candidates in Boötes gives 63%, 13% and 24% of the cases dominated by E, Sbc and Im templates, respectively. We note here that an E galaxy SED template does not directly imply that the galaxy morphology is elliptical. As discussed below, sources with the E-type template also include spiral galaxies with prominent bulges. Overall, there is also a large fraction of objects (37% if we combine Sbc and Im) dominated by late-type templates, suggesting that while early-type hosts are common, the red AGN population is hosted by a mixture of galaxy types.

Second, we recall the morphological results from §3.3. There we found that 54% (20%) of red (blue) AGN have disks, while 32% (80%) are elliptical or point sources. This means that the red AGN sample is not dominated by typical red sequence galaxies, and that blue AGN have, in fact, a lower fraction of late-types than red AGN. These findings strongly suggest that it is unlikely that the clustering results are driven by host galaxy differences or selection bias. Instead, the observed differences in their correlation functions actually represents an intrinsic difference in the environments of type-1 and type-2 AGN. Furthermore, as discussed in §6, the increase in clustering while moving from blue cloud to red sequence galaxies is markedly smaller than the difference between blue and red AGN.

### 5.4. Sensitivity to Redshift Distribution

As the amplitude of  $w(\theta)$  will certainly change depending on the location and shape of the redshift distribution in any observed sample of galaxies, it is important to assess how sensitive our bias estimates are to changes in the redshift distribution.

For this purpose we fit different model distributions for red and blue AGN redshifts and investigate how much the inferred absolute bias would change by systematically varying the distribution parameters with respect to the best-fitting case. To describe our redshifts, we adopt the Gamma statistical distribution of parameters  $\alpha$  (shape) and  $\beta$  (scale), although this choice is not critical (e.g. using Gaussians will lead to variations of the same order of magnitude). For red AGN the best-fit parameters to observed COSMOS redshifts are  $\alpha = 3.98$  and  $\beta = 0.22$

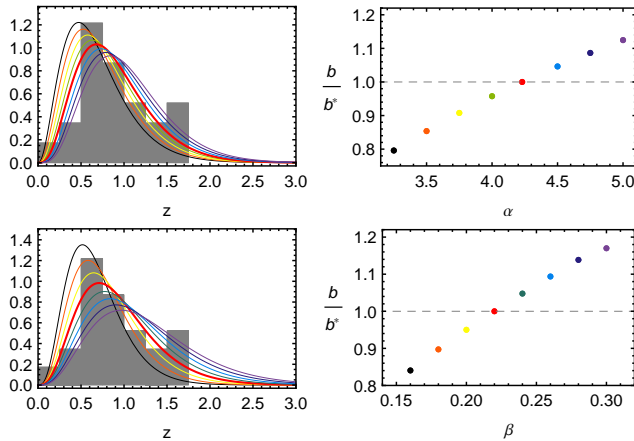


FIG. 14.— **Top row:** model redshift distributions of varying shape ( $\alpha$ ) parameter along with the corresponding change in absolute bias normalized to the best-fitting case (red thick line) to COSMOS spectroscopic data for red AGN (solid histogram). **Bottom row:** same as before but for distributions of varying scale ( $\beta$ ) parameter.

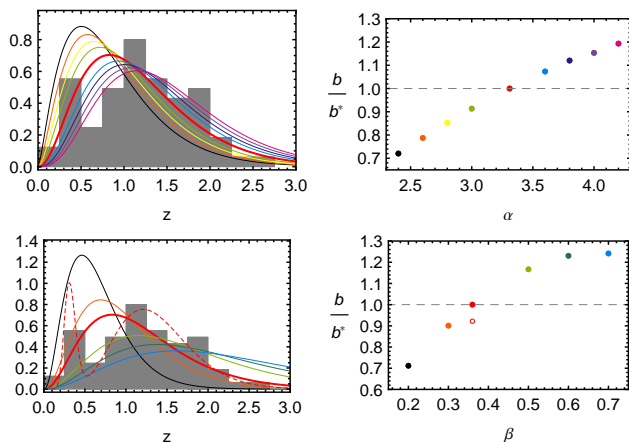


FIG. 15.— Same as Figure 14, but for the blue AGN sample. In addition, the bottom panels show the fit of a double Gamma distribution (dashed red line) along with the change in absolute bias (empty circle) with respect to the single distribution case.

( $\langle z \rangle = 0.88$ ), while for blue AGN we obtain  $\alpha = 2.65$  and  $\beta = 0.39$  ( $\langle z \rangle = 1.03$ ).

For our red AGN sample, in Figure 14 we reproduce the different model distributions with varying  $\alpha$  (top row) and  $\beta$  (bottom row), and the corresponding effect on the bias, always normalized to the best-fitting case highlighted in red. Changing  $\alpha$  or  $\beta$  within the range shown means that the bias could change by  $\sim 20\%$  at most. Note that to estimate  $b/b^*$  we assume a spatial correlation length  $r_0$  that is constant in redshift.

Figure 15 shows the same analysis applied to our blue AGN sample. The result is a similar variation of  $\sim 25\%$  in bias. In addition, we also test the effect of fitting a double Gamma distribution (dashed red line) instead of a single one. As expected, adding a second peak to the model naturally adjusts much better to the observed redshifts, yet the derived bias would decrease by only  $\sim 6\%$ . To further assess these conclusions, we repeated the test by directly convolving the COSMOS redshift distributions of blue and red AGN with a Gaussian kernel of increasing width. Once again the bias changes by about 30% for any reasonable broadening. Note that adopting

the Boötes redshift distributions as reference instead of COSMOS shifts these percentages by  $\lesssim 4\%$ , and so does not qualitatively alter our conclusions. Finally, a bias uncertainty of  $\sim 20\%$  in the *least favorable* scenario — e.g., the blue AGN bias is underestimated by 20%, while the red AGN bias is overestimated by 20% — still translates into systematic halo mass estimates a factor of  $\sim 3$  larger for red AGN than for blue AGN.

## 6. DISCUSSION

In this work we have taken advantage of recently released data from *WISE* to construct a large sample of  $\sim 170,000$  mid-IR-selected AGN candidates with the main purpose of analyzing their angular clustering properties. The selection is highly reliable ( $> 90\%$ ), as demonstrated in Stern et al. (2012) and Assef et al. (2013), as well as by the high rate of X-ray detections (§3.1). The median redshift of the sample is  $\langle z \rangle \sim 1.1$  based on relatively complete spectroscopy in the COSMOS and Boötes fields. By considering their optical counterparts from SDSS, we distinguish those *WISE*-selected AGN that are optically faint, and thus have red optical-to-mid-IR colors and are inferred to be heavily obscured AGN, from those that are optically bright, and thus have blue optical-to-mid-IR colors and are inferred to be unobscured AGN.

We find that, as a whole, the *WISE*-selected AGN population presents a similar clustering strength to optically selected quasars at comparable redshifts, with a slightly higher absolute bias with respect to the dark matter distribution for redder  $W1 - W2$  subsamples. We find that the red AGN show a notably larger bias level than that of blue AGN, with  $b = 2.9 \pm 0.6$  versus  $b = 1.6 \pm 0.6$  respectively. Using a significantly smaller sample of few hundred sources over a much smaller area, Hickox et al. (2011) reported a similar absolute bias of  $b = 2.87 \pm 0.77$  for obscured *Spitzer*-selected AGN. Our absolute bias estimates suggest that red AGN (*i.e.* obscured sources) are hosted by massive dark matter halos of  $\log(M/M_\odot h^{-1}) \sim 13.5$ , well above the halos of mass  $\log(M/M_\odot h^{-1}) \sim 12.4$  that harbor blue AGN (unobscured sources).

It is possible to interpret these results in a scenario where, at least during a brief phase before the dust is removed and the AGN gets “exposed”, the black hole mass is a factor of few below the  $M - \sigma$  relation of active galaxies. For our sample, from the SED fits of *WISE* AGN in Boötes we find that both red and blue AGN have similar distributions of AGN bolometric luminosity, with a nearly identical mean of  $\sim 2 \times 10^{12} L_\odot$ . This suggests that the black hole masses of our red and blue AGN do not differ much, and it is unlikely that their relative Eddington ratio is much different from unity. Moreover, their high luminosities are indicative of quasar-like accretion happening in both samples and we know that *WISE* AGN selection tends to pick up AGN radiating at large fractions of their Eddington limits (Assef et al. 2013). Since we find that obscured sources are hosted by more massive halos, then this means that, at least during a period of time, the black hole mass growth lags behind that of the hosting halos and hence the black holes in obscured AGN are temporarily “undermassive” until they reach their final mass. This is not entirely surprising, as, for example, Alexander et al. (2008) find that submillimeter



galaxies at  $z = 2$  host black holes  $\sim 10$  times smaller than the expected for radio galaxies and quasars.

The basis of such a lag argument for AGN has been proposed before in the literature (e.g., theoretically by King 2010, and coupled to clustering by Hickox et al. 2011). King (2010) suggests that the effect of Rayleigh-Taylor instabilities on the Eddington outflows that regulate black hole growth leads to black holes masses in active galaxies a factor a few below the  $M$ - $\sigma$  relation, assuming an observed AGN phase represents a black hole growth phase. Thus, AGN should recurrently reach Eddington-order luminosities in order to grow fast enough to reach the masses specified by the Soltan (1982) relation.

One popular scenario for obscured quasars is that they represent an early evolutionary stage of rapid black hole growth just before the emergence of an unobscured, optical quasar. Hopkins et al. (2008) pose that in the final stages of coalescence of the galaxies, massive inflows supply large amounts of gas, increasing the gas density around nuclear regions and feeding the black hole that: (1) initially is obscured, (2) grows accordingly at high Eddington rates, and (3) is small compared to the spheroid in formation. Then, any possible link between (final) black hole mass and halo mass (e.g. Ferrarese 2002) would predict DM halos of the same mass for obscured and unobscured sources. But, if obscured AGN are an early stage where black holes are acquiring their final mass, then they would inhabit more massive halos when compared to unobscured quasars of the same black hole mass.

The clustering of red and blue galaxies has been studied in detail by Coil et al. (2008) using DEEP2 survey data. They find that at  $z \sim 1$  the bias of blue cloud galaxies is in the range of  $b \sim 1.2 - 1.4$ . Moving towards the red sequence, the bias increases in about 30%, so the measured bias of red galaxies is  $b \sim 1.6 - 1.8$ . Our blue AGN candidates have a bias that is at least comparable to luminous blue DEEP2 galaxies or to their less luminous red galaxies, but the bias of *WISE* red AGN is much larger than that of red galaxies, and is well more than 30% greater than that of blue AGN. This suggests that our red AGN candidates do not seem to cluster like typical red sequence galaxies at these redshifts and that the change in clustering is intrinsic to the two AGN types. These results are in broad agreement with Hickox et al. (2009), who finds that mid-IR-selected AGN tend to reside in galaxies slightly bluer than the green valley; and with Griffith & Stern (2010), who conclude that the X-ray and mid-IR AGN are not dominated by early-type galaxies, but by later-type galaxies with disks.

Finally, our results allow to test a basic assumption of

the AGN unification paradigm. A fundamental prediction of orientation-driven AGN unification models is that the angular clustering strength should be similar for obscured and unobscured AGN. We find evidence that obscured AGN are, in fact, more clustered than unobscured sources, which would appear to make simple orientation, or obscuring torus scenarios much less plausible, or, at least, not the full story for AGN obscuration. Alternatively, it would be interesting to compare our results against predictions of more physical AGN models, where, for example, the sublimation radius changes with AGN power or the covering fraction depends on other physical parameters. Our data set does not allow us to test these models in detail, but larger samples with improved redshifts and spectral coverage will make it possible. Our primary result is a significant difference in the clustering of optically bright (blue) and optically faint (red) mid-IR-selected AGN, implying that, on average, obscured and unobscured AGN reside in different halos. This surprising result has important implications for AGN unification, the role of AGN feedback in galaxy formation, the lifetime of quasars, and for understanding the sources responsible for the cosmic X-ray background and their cosmic evolution.

We thank A. Myers for useful replies to questions and extend our gratitude to the *WISE* extragalactic science team for its continuous support and interesting discussions over the years. We also gratefully acknowledge the anonymous referee and numerous colleagues including G. Hasinger and R. Hickox who provided insightful comments that have improved our discussion. This publication makes use of data products from the *Wide-field Infrared Survey Explorer*, which is a joint project of the University of California, Los Angeles, and the Jet Propulsion Laboratory/California Institute of Technology, funded by the National Aeronautics and Space Administration. Funding for the SDSS and SDSS-II has been provided by the Alfred P. Sloan Foundation, the Participating Institutions, the National Science Foundation, the US Department of Energy, the National Aeronautics and Space Administration, the Japanese Monbukagakusho, the Max Planck Society and the Higher Education Funding Council for England. The SDSS website is <http://www.sdss.org/>. R.J.A. was supported in part by an appointment to the NASA Postdoctoral Program at the Jet Propulsion Laboratory, administered by Oak Ridge Associated Universities through a contract with NASA. R.J.A. was also supported in part by Gemini grant number 32120009. We also thank the NASA Astrophysics Data Analysis Program (ADAP) for its support.

## REFERENCES

- Abazajian K. N., Adelman-McCarthy J. K., Agueros M. A., et al., 2009, *ApJS*, 182, 543  
 Alexander D.M. et al., 2008, *AJ*, 135, 1968  
 Antonucci R.R.J., 1993, *ARA&A*, 31, 473  
 Assef R. J. et al., 2010, *ApJ*, 713, 970  
 Assef R. J. et al., 2013, *ApJ*, 772, 26  
 Best P.N., Kauffmann G., Heckman T.M., Brinchmann J., Charlot S., Ivezić Ž., White S.D.M., 2005, *MNRAS*, 362, 25  
 Brusa M., Civano F., Comastri A. et al., 2010, *ApJ*, 716, 348  
 Carroll S. M., Press W. H., Turner E. L., 1992, *ARA&A*, 30, 499  
 Coil A.L. et al., 2008, *ApJ*, 672, 153  
 Coil A.L. et al., 2009, *ApJ*, 701, 1484  
 Croom S.M. et al., 2004, *MNRAS*, 349, 1397  
 Croom S.M. et al., 2005, *MNRAS*, 356, 415  
 Cutri R. et al., 2011, *WISE Explanatory Supplement*.  
 Donley J.L., Koekemoer A.M., Brusa M. et al., 2012, *ApJ*, 748, 143  
 Donoso E., Li Cheng, Kauffmann G., Best P.N., Heckman, T.M., 2010, *MNRAS*, 407, 107  
 Eisenstein, D. J., Hu, W. 1998, *ApJ*, 496, 605  
 Elvis M., Civano F., Vignali C. et al., 2009, *ApJS*, 184, 158  
 Falder J. T., Stevens J. A., Jarvis M. J., 2010, *MNRAS*, 405, 347

- Ferrarese L., 2002, ApJ, 578, 90  
Georgakakis A. et al., 2007, ApJ, 660, 15  
Gilli R. et al., 2005, A&A, 430, 811  
Gilli R. et al., 2009, A&A, 494, 33  
Griffith R.L., Stern D., 2010, AJ, 140, 533  
Hasinger G. et al., 2007, ApJS, 172, 29  
Heisler C.A., Lumsden S.L., Bailey J.A. 1997, Nature, 385, 700  
Hickox R.C. et al., 2007, ApJ, 671, 1365  
Hickox R.C. et al., 2009, ApJ, 696, 891  
Hickox R.C. et al., 2011, AJ, 731, 117  
Hopkins P. et al., 2008, ApJS, 175, 356  
Jannuzi B. et al., 2010, Bulletin of the American Astronomical Society Meeting 215, Vol 42., p.513  
Jarrett T. et al., 2011, ApJ, 735, 112  
King A.R., 2010, MNRAS, 408, 95  
Kirkpatrick J.D. et al., 2011, ApJS, 197, 19  
Kochanek C. et al., 2012, ApJS, 200, 8  
Lacy M. et al., 2004, ApJS, 154, 166  
Landy S.D., Szalay A.S., 1993, ApJ, 412, 64  
Limber D.N., 1953, ApJ, 117, 134  
Martínez-Sansigre A. et al., 2009, ApJ, 706, 184  
Matthews T.A., Morgan W.W., Schmidt M., 1964, ApJ, 140, 35  
Myers A.D. et al., 2006, ApJ, 638, 622  
Myers A.D., Brunner R.J., Nichol R.C., Richards G.T., Schneider D.P., Bahcall N.A., 2007, ApJ, 658, 85  
Navarro J. F., Frenk C. S., White S. D. M., 1997, ApJ, 490, 493  
Peacock J.A., Dodds S.J., 1996, MNRAS, 280, 19  
Peebles P. J. E., 1980, The Large-scale Structure of the Universe. Princeton University Press, Princeton  
Richards G. T. et al., 2002, AJ, 124, 1  
Richards G. T. et al., 2004, ApJS, 155, 257  
Ross N.P. et al., 2009, ApJ, 697, 1634  
Schlegel D. J., Finkbeiner D. P., Davis M., 1998, AJ, 500, 525  
Shen Y. et al., 2001, AJ, 697, 1656  
Sheth, R. K., Mo, H. J., Tormen, G., 2001, MNRAS, 323, 1  
Soltan A., 1982, MNRAS, 200, 115  
Stern D., Djorgovski S.G., Perley R., de Carvalho R., Wall J. et al., 2000, AJ, 119, 1526  
Stern D. et al., 2005, ApJ, 631, 163  
Stern D. et al., 2012, AJ, 753, 30  
Stoughton C. et al., 2002, AJ, 123, 485  
Strauss M. A. et al., 2002, AJ, 124, 1810  
Tasse C., Röttgering H., Best P.N., 2011, A&A, 525, 127  
Trump J.R. et al., 2007, ApJS, 172, 383  
Urry C.M., Padovani P., 1995, PASP, 107, 803  
Verde L. et al., 2002, MNRAS, 335, 432  
Wright E. L. et al., 2010, AJ, 140, 1868  
Wylezalek D., Galametz A., Stern D. et al., 2013, ApJ, 769, 79  
Yan L. et al., 2013, AJ, 145, 55  
York D. G. et al., 2000, AJ, 120, 1579